Nanoscale

ROYAL SOCIETY OF CHEMISTRY

PAPER

View Article Online
View Journal | View Issue



Cite this: *Nanoscale*, 2021, **13**, 17093

# Observation of quantum-confined exciton states in monolayer $WS_2$ quantum dots by ultrafast spectroscopy†

Shu-Wen Zheng,[a] Lei Wang, *[a] Hai-Yu Wang, *[a] Chen-Yu Xu,[a] Yang Luo[b] and Hong-Bo Sun [c]

Monolayer transition metal dichalcogenide quantum dots (TMDC QDs) could exhibit unique photophysical properties, because of both lateral quantum confinement effect and edge effect. However, there is little fundamental study on the quantum-confined exciton dynamics in monolayer TMDC QDs, to date. Here, by selective excitations of monolayer $WS_2$ QDs in broadband transient absorption (TA) spectroscopy experiments, the excitation-wavelength-dependent ground state bleaching signals corresponding to the quantum-confined exciton states are directly observed. Compared to the time-resolved photophysical properties of $WS_2$ nanosheets, the selected monolayer $WS_2$ QDs only show one ground state bleaching peak with larger initial values for the linear polarization anisotropy of band-edge excitons, probably due to the expired spin–orbit coupling. This suggests a complete change of the band structure for monolayer $WS_2$ QDs. In the femtosecond time-resolved circular polarization anisotropy experiments, a valley depolarization time of ~100 fs is observed for $WS_2$ nanosheets at room temperature, which is not observed for monolayer $WS_2$ QDs. Our findings suggest a strong state-mixing of band-edge valley excitons responsible for the large linear polarization in monolayer $WS_2$ QDs, which could be helpful for understanding the exciton relaxation mechanisms in colloidal monolayer TMDC QDs.

Received 27th July 2021,
Accepted 17th September 2021

DOI: 10.1039/d1nr04868f

rsc.li/nanoscale



## Introduction

Two-dimensional (2D) transition metal dichalcogenides (TMDCs) (such as $MoS_2$, $WS_2$, $WSe_2$, *etc.*) are promising building blocks for fabricating next-generation electronic, optoelectronic and valleytronic devices due to their extraordinary properties.[1–3] First of all, 2D TMDCs have optical band gaps in the visible to near infrared band, which are suitable for photodetectors and photocatalysis.[4] Secondly, unlike their indirect-band gap bulk counterparts, monolayer TMDCs further exhibit direct band gaps and optical transparency and are promising candidates in thin film transistors and solar cells.[5,6] Last but not least, strong spin orbit coupling and lack of inversion symmetry in 2D TMDCs result in valley-selective optical properties, providing a new degree of freedom to control the materials properties.[7–9] Therefore, 2D TMDCs also possess huge potential for valleytronics.

The lateral dimension of the 2D TMDCs can be further reduced into nanosheets or quantum dots (QDs), which provides a new method to adjust the electronic band structures of 2D TMDCs.[10,11] 2D TMDC nanosheets and QDs are expected to not only have the intrinsic properties of the TMDC materials, but also may exhibit different photophysical properties of their film materials, because of the additional quantum confinement effect in lateral dimension and the edge effect, which could extend their applications in catalysis and biological aspects.[12] For example, the good dispersion and chemical stability of 2D TMDC QDs are suitable for biological imaging and cancer physiotherapy.[13,14] Besides, a large number of edge active sites of TMDC QDs are applicable to the field of catalysis.[15,16] Wu's group has successfully synthesized $MoS_2$ and $WS_2$ QDs through the solvothermal treatment, and characterize their steady-state absorption and photoluminescence properties, where the strong fluorescence of TMDC QDs under UV light irradiations has been reported.[10] Son's group and Cheon's group have developed a new method to produce highly uniform monolayer $WS_2$ QDs, showing well-defined photoluminescence spectra without ensemble heterogeneity,

[a]*State Key Laboratory of Integrated Optoelectronics, College of Electronic Science and Engineering, Jilin University, 2699 Qianjin Street, Changchun 130012, China. E-mail: haiyu_wang@jlu.edu.cn*
[b]*Changchun Institute of Optics, Fine Mechanics and Physics, Chinese Academy of Sciences, Changchun 130033, China*
[c]*State Key Laboratory of Precision Measurement Technology and Instruments, Department of Precision Instrument, Tsinghua University, Haidian, Beijing 100084, China*

†Electronic supplementary information (ESI) available. See DOI: 10.1039/d1nr04868f

and observed that solvents have a strong influence on the optical properties of TMDC QDs.[11,17] However, there is little fundamental study on the quantum-confined exciton dynamics in monolayer TMDC QDs to date, which would hinder the further development of the optoelectronic applications based on 2D TMDC QDs.

In this paper, we use broadband femtosecond transient absorption (TA) spectroscopy to selectively excite monolayer $WS_2$ QDs in the visible region. The excitation-wavelength-dependent ground state bleaching signals corresponding to the quantum-confined exciton states are directly observed in monolayer $WS_2$ QDs. Compared to multiple-exciton-state $WS_2$ nanosheets, only one ground state bleaching peak with large initial values for the linear polarization anisotropy for band-edge excitons of selected monolayer $WS_2$ QDs implies a complete change of the band structure. We further find that the valley depolarization time of $WS_2$ nanosheets is ~100 fs at room temperature, and the valley polarization for monolayer $WS_2$ QDs is not observed. Our findings could be helpful for understanding the exciton relaxation mechanisms in colloidal monolayer TMDC QDs.

## Experimental

### Sample preparation

The $WS_2$ nanosheets and monolayer $WS_2$ QDs were synthesized by a modified solvothermal method.[10] Typically, 0.1 g of $WS_2$ powder (2 μm, 99% Sigma-Aldrich) was added into 10 ml *N*-methylpyrrolidone (NMP) first, and it was sonicated using a cell disruptor for 3 hours with an output power of 300 W. In order to avoid high temperature during the ultrasonic treatments, ice bath conditions were required. When the sonication procedure was completed, the supernatant of $WS_2$ dispersion was centrifuged at 1500 rpm for 45 minutes, and the top 3/4 of the dispersion was collected. Then, it was further centrifuged at 200 rpm for 45 minutes, and the top 1/2 of this dispersion was labeled as $WS_2$ nanosheets. The dispersion of $WS_2$ nanosheets was transferred into a flask and vigorously stirred for 6 hours at 140 °C. Finally, the resulting supernatant was centrifuged for 5 minutes at 3500 rpm to obtain monolayer $WS_2$ QDs.

**Steady-state characterization.** The steady-state absorption spectra and photoluminescence (PL) spectra were measured using a spectrophotometer Shimadzu UV-2550 and FL-4600, respectively. The thicknesses of $WS_2$ nanosheets and $WS_2$ QDs were measured by atomic force microscopy (AFM, Bruker Corporation) in the tapping mode. X-ray diffraction (XRD) data were recorded on a Rigaku D/Max-2550 diffractometer with Cu Kα radiation ($\lambda$ = 0.15418 nm).

**Femtosecond broadband TA system.** We used a mode-locked Ti:sapphire amplifier to generate 800 nm (repetition rate: 500 Hz) laser pulses with 35 fs pulse width (Solstice, Spectra-Physics). It was split into two beams through an 80% (reflection)/20% (transmittance) mirror: one stronger beam passed through the TOPAS system to produce the excitation lights (470 nm, 570 nm and 610 nm); the other was through 2 mm water, producing a broadband probe light (ranging from 400 nm to 800 nm). The TA signals were collected using a fiber-coupled spectrometer. The dispersion correction of TA data was performed using the CHIRP program. All TA experiments were performed at room temperature.

## Results and discussion

Fig. 1a shows the transmission electron microscopy (TEM) images of $WS_2$ QDs, whose average size is 2.8 ± 0.9 nm, and the *d*-spacing is 2.7 Å corresponding to the (101) face of $WS_2$. The thickness of $WS_2$ QDs is ~1 nm, according to the height profile shown in AFM images (Fig. S1a†). This suggests that most of the $WS_2$ QDs are monolayers[10] and their lateral dimension is comparable with the exciton Bohr radius of TMDC monolayers.[18] For $WS_2$ nanosheets, the thickness is ~3 nm and the lateral size is ~200 nm, according to the scanning electron microscopy (SEM) image (Fig. S2†), which is consistent with the AFM image of $WS_2$ nanosheets (Fig. S1b†). Besides, we characterize the X-ray powder diffraction (XRD) spectra of $WS_2$ nanosheets and QDs (Fig. S3†). $WS_2$ nanosheets have a characteristic XRD peak at $2\theta = 14.4°$ for the (002) reflection, while $WS_2$ QDs exhibit no apparent XRD peak. The disappearance of the (002) reflection in the XRD patterns of TMDCs could occur when the layer number reduces from multilayer to monolayer.[19] This further indicates that the synthesized $WS_2$ nanosheets are multilayer, and $WS_2$ QDs are mainly monolayer. The steady-state absorption spectrum of $WS_2$ nanosheets shows four absorption peaks, which locates at 634 nm, 527 nm, 457 nm and 416 nm, respectively (Fig. 1b). The absorption peaks at 634 nm and 527 nm for $WS_2$ nanosheets are attributed to the direct transitions at the K point, while the other absorption peaks at 457 nm and 416 nm are assigned to the indirect transitions at band-nesting areas between Γ and Q valleys in band structures.[20] But all the typical exciton absorption peaks for $WS_2$ nanosheets also disappear in monolayer $WS_2$ QDs, which only show a smooth and structureless absorption curve in the UV-vis-near infrared spectral range. This could be attributed to the size-distribution effect for monolayer $WS_2$ QDs, and the change of band structure induced by quantum confinement.[21] Fig. 1c shows the PL spectra of monolayer $WS_2$ QDs under different excitation wavelengths (there is no PL signals for $WS_2$ nanosheets). As the excitation wavelength increases from 350 nm to 380 nm, the PL intensity of monolayer $WS_2$ QDs increases and its maximum value locates at 445 nm. When the excitation wavelength is further increased from 380 nm to 470 nm, the PL peaks of monolayer $WS_2$ QDs gradually shift from 450 nm to 530 nm, exhibiting an excitation wavelength-dependent behavior.[10] The multiple-peak PL of monolayer $WS_2$ QDs could be related to the vibronic coupling states that might come from edge bonds.[11] The PL excitation (PLE) spectra of monolayer $WS_2$ QDs (Fig. 1d) also could reflect the exciton fine structures of corresponding PL peaks. The two PLE peaks at 320 nm and

 

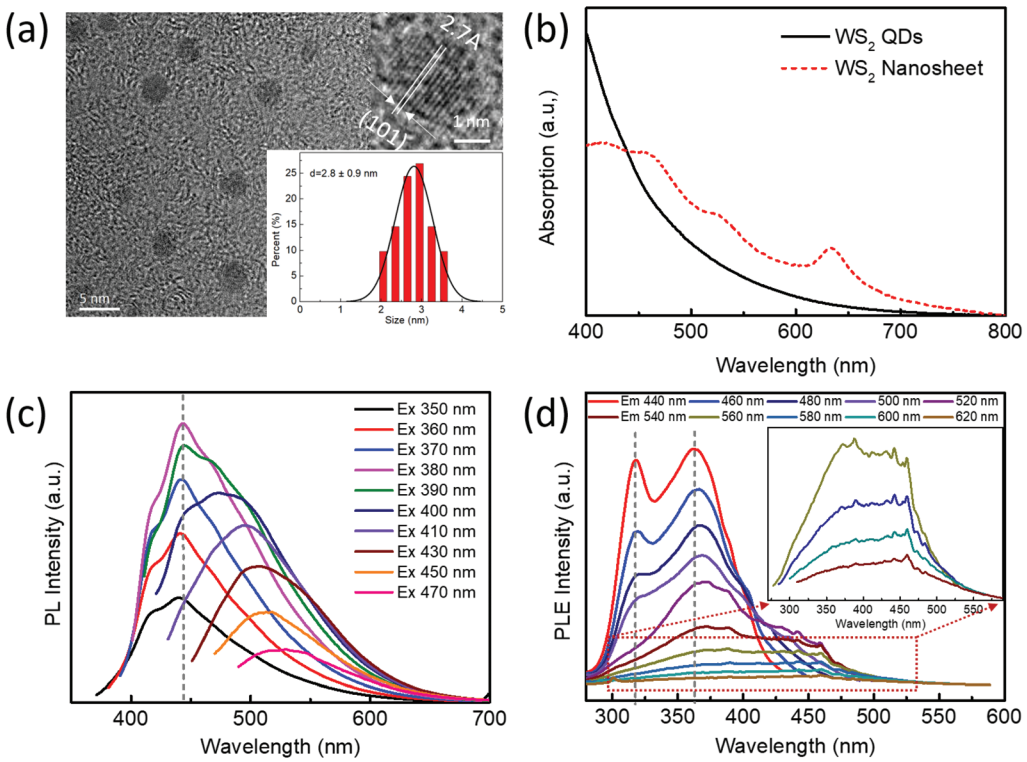


**Fig. 1** (a) High resolution transmission electron microscopy (HRTEM) image of monolayer $WS_2$ QDs. The inset of panel (a) is the size distribution of monolayer $WS_2$ QDs. (b) Steady-state absorption spectra of the $WS_2$ nanosheet and monolayer $WS_2$ QDs in NMP. (c) Steady-state PL spectra of monolayer $WS_2$ QDs in NMP under different excitation wavelengths. The vertical dashed line indicates the PL peak at 445 nm. (d) Corresponding PLE spectra for monolayer $WS_2$ QDs in NMP probed at different emission wavelengths. The vertical dashed lines indicate the PLE peaks at 320 nm and 360 nm, respectively.

360 nm in the UV range are responsible for the relatively stronger blue emissions (440–480 nm) of monolayer $WS_2$ QDs. For the relatively weaker green and red emissions (500–620 nm) of monolayer $WS_2$ QDs, the PLE spectra are broad and the contributions of the PLE peak at 320 nm and 360 nm become smaller and smaller, as the detection wavelengths gradually red-shift. This implies the size-distribution effect for monolayer $WS_2$ QDs.

In order to reveal the underlying quantum-confined effects in monolayer $WS_2$ QDs, selective-excitation TA experiments are performed. Fig. 2 shows the TA spectra of monolayer $WS_2$ QDs under different excitation wavelengths. We use 470 nm, 570 nm, and 610 nm pump lights to selectively excite the relatively large $WS_2$ QDs (considering our sample has a size distribution of 2.8 ± 0.9 nm). The relatively small $WS_2$ QDs may have the main absorption peaks in the spectral range of <400 nm, which are beyond our probe window. The state filling caused by the transition of ground electrons to the excited states will lead to the generation of ground state bleaching (GSB) signals, which are the negative signals in our TA spectra. The positive signals are typically assigned to the excited-state absorption (ESA) signals.[22,23] All the observed GSB peaks for monolayer $WS_2$ QDs are located around the chosen excitation wavelengths, demonstrating that there are quantum-confined states.[24] Since the pump fluences for those TA experiments are under control (all pump fluences are ~25 μJ $cm^{-2}$), the decreased intensity of the GSB signals observed in Fig. 2 with increasing excitation wavelength indicates a smaller number of nanoparticles for larger $WS_2$ QDs. Instead, the TA spectra of $WS_2$ nanosheets show the narrower GSB signals for the band-edge A-exciton (632 nm) and B-exciton (525 nm) under the same excitation conditions pumped by 610 nm pulses (Fig. S4†). The difference between TA spectra of monolayer $WS_2$ QDs and $WS_2$ nanosheets indicates a dramatic change of the band structure at the K point for $WS_2$ QDs.

Fig. 2d compares the band-edge exciton dynamics between $WS_2$ nanosheets and monolayer $WS_2$ QDs. For $WS_2$ nanosheets, the A-exciton resonant excitation at 610 nm results in the photogeneration of exciton distribution close to the K point in an indirect band gap structure, in which those excitons have to experience fast non-radiative recombination processes. For the band-edge exciton dynamics of selected monolayer $WS_2$ QDs, although those quantum-confined exciton states are obtained from the size-selective excitations, their decay rates are almost the same, and remarkably slower than that of $WS_2$ nanosheets. This indicates that those relatively large $WS_2$ QDs with a direct band gap structure could undergo the same exciton relaxation pathway and exhibit the resulting radiative recombination behaviors. The dynamics of

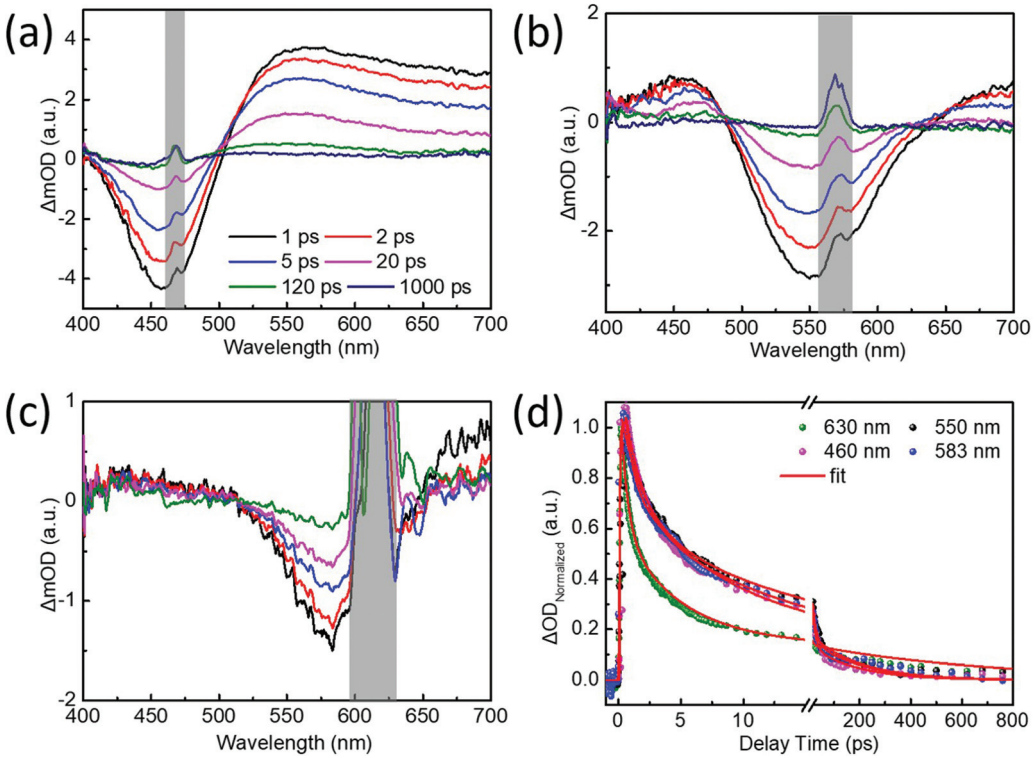


**Fig. 2** TA spectra of monolayer $WS_2$ QDs under (a) 470 nm, (b) 570 nm, and (c) 610 nm excitation, respectively, probed at different delay times. The values of ΔOD are equal to the changes of absorption, when it is excited with and without pump light. OD, optical density. (d) Normalized dynamics of band-edge excitons probed at 460 nm, 550 nm and 583 nm for monolayer $WS_2$ QDs at 470 nm, 570 nm, and 610 nm excitation wavelengths, respectively, in comparison with that probed at 630 nm for $WS_2$ nanosheets under 610 nm excitation. The shadow areas in panel (a–c) are from the scattering of excitation lights.

exciton decay of monolayer $WS_2$ QDs and $WS_2$ nanosheets can be well fitted by a multi-exponential decay function: $I(t) = A_i \exp(-t/\tau_i)$. For $WS_2$ nanosheets, there are three lifetimes, 0.57 ± 0.01 ps (46%), 4.9 ± 0.1 ps (41%) and 703 ± 30 ps (13%). For monolayer $WS_2$ QDs, for example those under 470 nm excitation, the fitted lifetimes are 1.4 ± 0.1 ps (37%), 12 ± 1 ps (50%) and 184 ± 14 ps (13%). All the best-fitted parameters shown in Fig. 2d are presented in Table S1.† The first two lifetime components are usually attributed to the trapping or scattering processes of TMDCs.[25] The slowest lifetime component in $WS_2$ nanosheets could be assigned to the indirect recombination of electrons and holes. For monolayer $WS_2$ QDs, the slowest lifetime component could be related to the radiative recombination processes,[26] which is consistent with the multi-exponential fitting results of time-resolved PL dynamics of monolayer $WS_2$ QDs (Fig. S5†), where the fastest PL decay component is ~0.16 ns.

We further investigate the linearly and circularly polarized exciton dynamics for monolayer $WS_2$ QDs and $WS_2$ nanosheets. Fig. 3a and c present the TA spectra of monolayer $WS_2$ QDs and $WS_2$ nanosheets, respectively, under the conditions that the polarization direction of probe lights is parallel ($I_{\parallel}$) or perpendicular ($I_{\perp}$) to that of excitation light. The linear polarization anisotropy is defined as $r = (I_{\parallel} - I_{\perp})/(I_{\parallel} + 2I_{\perp})$.[27] Fig. 3b and Fig. S6† show the initial anisotropy spectra of $WS_2$ nanosheets and monolayer $WS_2$ QDs, respectively. When the overlapping areas between the negative GSB and positive ESA signals in the TA spectra appear around the crossing points of ΔOD = 0, it will lead to infinite anisotropy values in the anisotropy spectra, which should be ignored. This indicates a strong linear polarization for the band-edge exciton state of selected monolayer $WS_2$ QDs, which are much larger than that of $WS_2$ nanosheets. Since the maximum theoretical anisotropy is 0.4 for a system with random distribution of linear polarization orientation,[8] which has been verified here by the linearly polarized anisotropy TA experiments for the aqueous solution of rhodamine B under 520 nm excitation too (it is $r \approx 0.4$ probed at 0.2 ps, and $r = 0.34$ probed at 1 ps; the grey dashed line in Fig. 3d shows its anisotropic dynamics, which demonstrates that there is no artifactual anisotropy component in our measurement system), it is quite interesting that there is a remarkably high initial anisotropy value of 0.59 at ~1 ps (probed at 510 nm; the black line in Fig. 3d and it might be larger if probed at 0.2 ps) for monolayer $WS_2$ QDs, for example, under 520 nm excitation. Such large initial linear polarization anisotropy for band-edge excitons of selected monolayer $WS_2$ QDs could be a result of band structure change, like expired spin–orbit coupling, since the lateral quantum confinement effect in monolayer $WS_2$ QDs would enforce a strong state-mixing on the original 'A-exciton' and

 

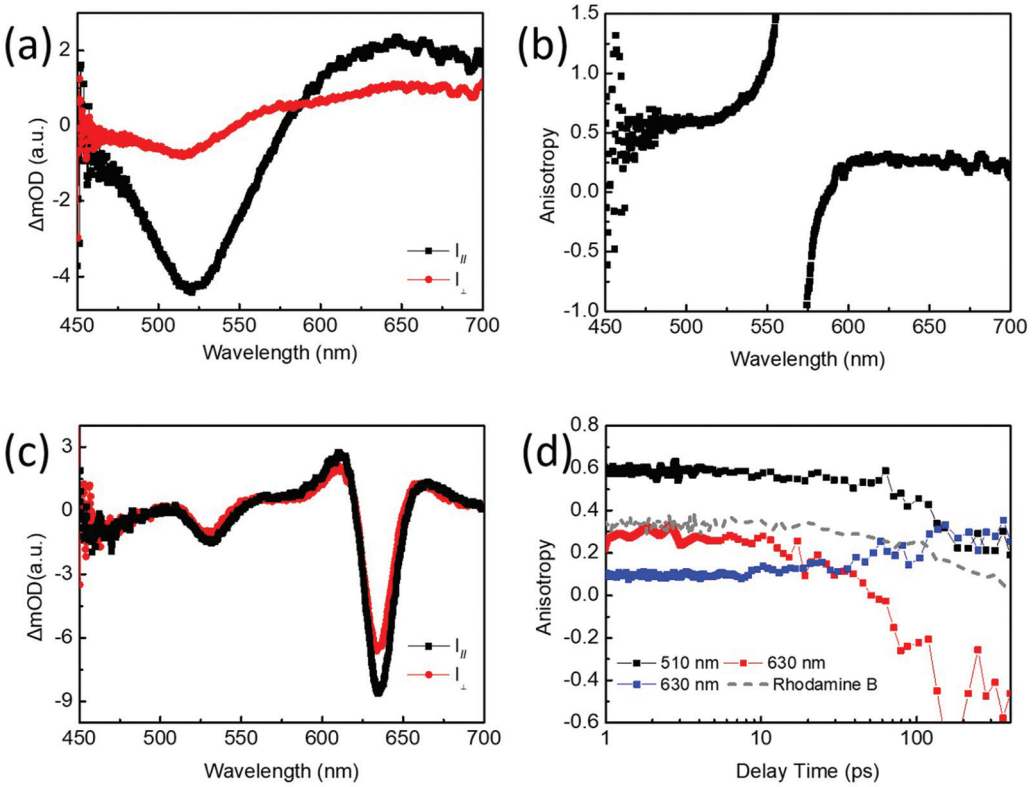


**Fig. 3** (a) Parallel and perpendicular TA spectra of monolayer $WS_2$ QDs under 520 nm excitation probed at 1 ps. (b) Anisotropic spectrum of monolayer $WS_2$ QDs probed at 1 ps. (c) Parallel and perpendicular TA spectra of $WS_2$ nanosheets under 610 nm excitation probed at 0.28 ps. (d) Anisotropic dynamics of monolayer $WS_2$ QDs under 520 nm excitation probed at 510 nm (black line) and 630 nm (red line); anisotropic dynamics of $WS_2$ nanosheets under 610 nm excitation probed at 630 nm (blue line). The grey dashed line represents the anisotropy dynamics of rhodamine B under 520 nm excitation probed at 560 nm.

'B-exciton' states observed in $WS_2$ nanosheets or monolayer $WS_2$ films. This would lead to the 'degenerate states' at the band edge of monolayer $WS_2$ QDs, which corresponds to the observed broad GSB peak and exhibits large initial values for the linear polarization anisotropy as a coherent superposition of valley excitons.[28–32] This might be further affected by the signal superposition of monolayer $WS_2$ QDs with similar sizes, or the other factors like the so-called solvent-QD interactions.[16] The time-resolved PL anisotropy dynamics of monolayer $WS_2$ QDs is measured, which presents a single exponential decay of 1.3 ns, corresponding to a rotational diameter of ~1.4 nm (see details in Fig. S7†).[33] It is worth noting that the initial PL anisotropy value for monolayer $WS_2$ QDs is ~0.16 probed at 0.4 ns, in agreement with the anisotropic value of ~0.19 for the band-edge exciton state obtained from the TA experiment recorded at 400 ps. This suggests that there is actually a minor effect of signal superposition for monolayer $WS_2$ QDs with different sizes on the linear polarization anisotropy values. In addition, the linear polarization dynamics for the ESA part (probed at 630 nm; the red line in Fig. 3d) of monolayer $WS_2$ QDs shows a switching process from the positive value of 0.27 at ~1 ps to a negative value of −0.45 after 100 ps. Its decay trend is also different from that observed at 510 nm (Fig. S8†). Together with the calculated rotational diameter, which is slightly larger than the physical thickness of monolayer $WS_2$ QDs, both the facts mentioned above imply the influence of the solvent on rotational diffusion behavior and linear polarization of monolayer $WS_2$ QDs. Furthermore, according to our observations, there could be two electronic states in monolayer $WS_2$ QDs. One is responsible for the size-dependent PL of monolayer $WS_2$ QDs, which is the intrinsic state corresponding to the GSB peak; and the other could be affected by the solvent environment, which is assigned to the edge state, corresponding to the ESA part in the red-side of the GSB signal. On the other hand, the initial linear polarization anisotropy for the band-edge A-exciton of $WS_2$ nanosheets under 610 nm excitation is only ~0.1, maintained for ~10 ps. Then, it gradually increases to 0.33 at ~150 ps. Finally, it begins to decay very slowly (probed at 630 nm; the blue line in Fig. 3d). The complex linear anisotropic dynamics indicates the heterogeneity of $WS_2$ nanosheets, which may contain small monolayers attached to larger and thicker multilayer nanosheets.

TA spectra of monolayer $WS_2$ QDs and $WS_2$ nanosheets under the same circularly polarized (SCP) and opposite circularly polarized (OCP) conditions for the pump and probe lights are presented in Fig. 4. The degree of valley polarization is defined as $P(\lambda,t)=\frac{\Delta OD_{SCP}(\lambda,t)-\Delta OD_{OCP}(\lambda,t)}{\Delta OD_{SCP}(\lambda,t)+\Delta OD_{OCP}(\lambda,t)}$. There is no

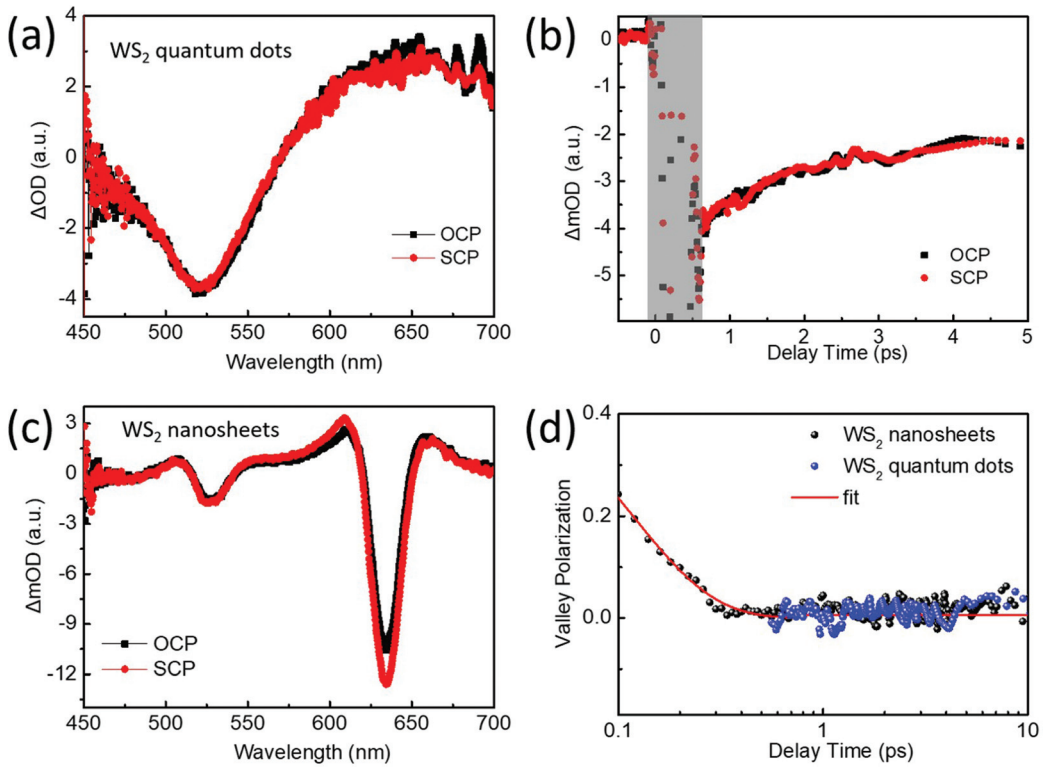


**Fig. 4** (a) TA spectra of monolayer $WS_2$ QDs probed at 1 ps delay times with SCP and OCP configurations under 520 nm excitation. (b) The SCP and OCP dynamics of A exciton probed at 520 nm of monolayer $WS_2$ QDs. The shadow area shows the disturbance from the scattering of excitation lights. (c) TA spectra of $WS_2$ nanosheets probed at 0.25 ps in SCP and OCP configurations under 610 nm excitation. (d) Valley polarization dynamics of monolayer $WS_2$ QDs under 520 nm excitation and $WS_2$ nanosheets under 610 nm excitation.

distinction between the SCP and OCP signals for monolayer $WS_2$ QDs in the circularly polarized TA spectra and corresponding dynamics (Fig. 4a and b). $WS_2$ nanosheets show larger SCP signals than the OCP signals at the band-edge A-exciton state (Fig. 4c). These SCP and OCP dynamics of A-exciton for $WS_2$ nanosheets are presented in Fig. S9.† Fig. 4d displays the valley polarization dynamics of $WS_2$ nanosheets and monolayer $WS_2$ QDs. For $WS_2$ nanosheets, the valley depolarization lifetime is 108 ± 6 fs, which could be mainly attributed to the electron–hole exchange interaction and phonon-assisted intervalley scattering.[34] For monolayer $WS_2$ QDs, the circular polarization response is not observed here too, which could be mainly due to the change of the band structure, like the expired spin–orbit coupling. Besides, the lateral quantum confinement for $WS_2$ QDs enhances the solvent-QD interactions, which might further shorten the possible valley depolarization time, and make it beyond our detection limit of ~35 fs. Under our current experimental conditions, only a small part of the monolayer $WS_2$ QDs corresponding to the pump pulses are selectively excited, which absorbs parts of pump lights, and the remaining excitation pulses will strongly interact with the solvents, generating undesired nonlinear signals within the initial probe times (the shadow area in Fig. 4b; this disturbance is much smaller in $WS_2$ nanosheets, since they exhibit larger absorption under their A-exciton resonance excitation than that of monolayer $WS_2$ QDs). This hinders the direct observation of the initially linear and circular depolarization processes of monolayer $WS_2$ QDs. Higher quality of monolayer $WS_2$ QDs with better lateral size distributions would be helpful for this investigation in the future.

## Conclusions

In conclusion, we have directly observed the quantum-confined exciton states in monolayer $WS_2$ QDs. Compared to $WS_2$ nanosheets, the selected monolayer $WS_2$ QDs only show one GSB peak for band-edge excitons and exhibit larger initial values for linear polarization anisotropy, all indicating a transition of the band structure for monolayer $WS_2$ QDs due to expired spin orbit coupling. The lost spin–orbit coupling in monolayer $WS_2$ QDs may be relevant to the changes in atomic arrangements (like curving in solution) or symmetry (like the broken $C3$-rotation symmetry), under strong quantum confinement in the lateral dimension. We also suggest that there could be a strong state-mixing of band-edge valley excitons in monolayer $WS_2$ QDs, which is responsible for the resulting large linear polarization. Instead, in femtosecond time-resolved circular polarization anisotropy experiments, no

 

obvious valley polarization is observed for monolayer $WS_2$ QDs, and an ultrafast valley depolarization time of ~100 fs for $WS_2$ nanosheets is recorded at room temperature. It needs more theoretical and time-resolved experimental investigation in the future for the electronic structure of monolayer $WS_2$ QDs, which could be affected by the coherent state-mixing due to the quantum confinement effects and the additional solvent-QD interactions.

## Author contributions

The manuscript was written through contributions of all authors. All authors have given approval to the final version of the manuscript.

## Conflicts of interest

There are no conflicts to declare.

## Acknowledgements

This work was supported by the National Key Research and Development Program of China and the National Natural Science Foundation of China (NSFC) under Grants #2017YFB1104300, #21773087, #21603083, #61927814, #21903035 and #22073037.

## References

1 X. Zong, H. Hu, G. Ouyang, J. Wang, R. Shi, L. Zhang, Q. Zeng, C. Zhu, S. Chen, C. Cheng, B. Wang, H. Zhang, Z. Liu, W. Huang, T. Wang, L. Wang and X. Chen, *Light: Sci. Appl.*, 2020, **9**, 114.
2 P. Zhang, C. Bian, J. Ye, N. Cheng, X. Wang, H. Jiang, Y. Wei, Y. Zhang, Y. Du, L. Bao, W. Hu and Y. Gong, *Sci. China Mater.*, 2020, **63**, 1548–1559.
3 Y. Liu, Y. Gao, S. Zhang, J. He, J. Yu and Z. Liu, *Nano Res.*, 2019, **12**, 2695–2711.
4 A. Splendiani, L. Sun, Y. Zhang, T. Li, J. Kim, C. Y. Chim, G. Galli and F. Wang, *Nano Lett.*, 2010, **10**, 1271–1275.
5 D. Wickramaratne, F. Zahid and R. K. Lake, *J. Chem. Phys.*, 2014, **140**, 124710.
6 C. Hu, X. Wang and B. Song, *Light: Sci. Appl.*, 2020, **9**, 88.
7 M. M. Glazov, E. L. Ivchenko, G. Wang, T. Amand, X. Marie, B. Urbaszek and B. L. Liu, *Phys. Status Solidi B*, 2015, **252**, 2349–2362.
8 J. R. Lakowicz, in *Principles of Fluorescence Spectroscopy*, Springer, New York, 3rd edn, 2006.
9 D. Xiao, G. B. Liu, W. Feng, X. Xu and W. Yao, *Phys. Rev. Lett.*, 2012, **108**, 196802.
10 S. Xu, D. Li and P. Wu, *Adv. Funct. Mater.*, 2015, **25**, 1127–1136.
11 H. Jin, M. Ahn, S. Jeong, J. H. Han, D. Yoo, D. H. Son and J. Cheon, *J. Am. Chem. Soc.*, 2016, **138**, 13253–13259.
12 L. Wang, Q. Li, H.-Y. Wang, J.-C. Huang, R. Zhang, Q.-D. Chen, H.-L. Xu, W. Han, Z.-Z. Shao and H.-B. Sun, *Light: Sci. Appl.*, 2015, **4**, e245–e245.
13 L. Yuwen, J. Zhou, Y. Zhang, Q. Zhang, J. Shan, Z. Luo, L. Weng, Z. Teng and L. Wang, *Nanoscale*, 2016, **8**, 2720–2726.
14 Y. Yong, T. Bao, M. Zu, L. Yan, W. Yin, C. Ge, D. Wang, Z. Gu, Y. Zhao and X. Cheng, *ACS Nano*, 2013, **9**, 12451–12463.
15 X. Zhao, X. Ma, J. Sun, D. Li and X. Yang, *ACS Nano*, 2016, **10**, 2159–2166.
16 X. Ren, L. Pang, Y. Zhang, X. Ren, H. Fan and S. Liu, *J. Mater. Chem. A*, 2015, **3**, 10693–10697.
17 H. Jin, B. Baek, D. Kim, F. Wu, J. D. Batteas, J. Cheon and D. H. Son, *Nano Lett.*, 2017, **17**, 7471–7477.
18 W. X. Yin, X. Bai, P. Chen, X. Y. Zhang, L. Su, C. Y. Ji, H. M. Gao, H. W. Song and W. W. Yu, *ACS Appl. Mater. Interfaces*, 2018, **10**, 43824–43830.
19 H. S. Matte, A. Gomathi, A. K. Manna, D. J. Late, R. Datta, S. K. Pati and C. N. Rao, *Angew. Chem., Int. Ed. Engl.*, 2010, **49**, 4059–4062.
20 V. Štengl, J. Tolasz and D. Popelková, *RSC Adv.*, 2015, **5**, 89612–89620.
21 C. Han, Y. Zhang, P. Gao, S. Chen, X. Liu, Y. Mi, J. Zhang, Y. Ma, W. Jiang and J. Chang, *Nano Lett.*, 2017, **17**, 7767–7772.
22 L. Wang, H.-Y. Wang, H.-T. Wei, H. Zhang, Q.-D. Chen, H.-L. Xu, W. Han, B. Yang and H.-B. Sun, *Adv. Energy Mater.*, 2014, **4**, 1301882.
23 H. Wang, H.-Y. Wang, Q.-D. Chen, H.-L. Xu, H.-B. Sun, F. Huang, W. Raja, A. Toma and R. Zaccaria, *Laser Photonics Rev.*, 2018, **12**, 1700176.
24 L. Wang, H. Y. Wang, Y. Wang, S. J. Zhu, Y. L. Zhang, J. H. Zhang, Q. D. Chen, W. Han, H. L. Xu, B. Yang and H. B. Sun, *Adv. Mater.*, 2013, **25**, 6539–6545.
25 H. Y. Shi, R. S. Yan, S. Bertolazzi, J. Brivio, B. Gao, A. Kis, D. Jena, H. G. Xing and L. B. Huang, *ACS Nano*, 2013, **7**, 1072–1080.
26 A. Granados Del Aguila, S. Liu, T. T. H. Do, Z. Lai, T. H. Tran, S. R. Krupp, Z. R. Gong, H. Zhang, W. Yao and Q. H. Xiong, *ACS Nano*, 2019, **13**, 13006–13014.
27 Y. Wang, L. Wang, H. Y. Wang, B. R. Gao and H. B. Sun, *J. Phys. Chem. Lett.*, 2020, **11**, 1483–1489.
28 K. F. Mak, D. Xiao and J. Shan, *Nat. Photonics*, 2018, **12**, 451–460.
29 Z. Ye, D. Sun and T. F. Heinz, *Nat. Phys.*, 2016, **13**, 26–29.
30 B. Zhu, H. Zeng, J. Dai, Z. Gong and X. Cui, Anomalously robust valley polarization and valley coherence in bilayer WS2, *Proc. Natl. Acad. Sci. U. S. A.*, 2014, **111**, 11606.
31 G. Wang, X. Marie, B. L. Liu, T. Amand, C. Robert, F. Cadiz, P. Renucci and B. Urbaszek, *Phys. Rev. Lett.*, 2016, **117**, 187401.
32 A. M. Jones, H. Yu, N. J. Ghimire, S. Wu, G. Aivazian, J. S. Ross, B. Zhao, J. Yan, D. G. Mandrus, D. Xiao, W. Yao and X. Xu, *Nat. Nanotechnol.*, 2013, **8**, 634–638.

33 L. Wang, S. J. Zhu, H. Y. Wang, Y. F. Wang, Y. W. Hao, J. H. Zhang, Q. D. Chen, Y. L. Zhang, W. Han, B. Yang and H. B. Sun, *Adv. Opt. Mater.*, 2013, **1**, 264–271.

34 R. Schmidt, G. Berghauser, R. Schneider, M. Selig, P. Tonndorf, E. Malic, A. Knorr, S. Michaelis de Vasconcellos and R. Bratschitsch, *Nano Lett.*, 2016, **16**, 2945–2950.